

The *Swift*/UVOT catalogue of NGC 4321 star forming sources: A case against density wave theory

Ignacio Ferreras^{1*}, Mark Cropper¹, Daisuke Kawata¹, Mat Page¹, Erik A. Hoversten²

¹ Mullard Space Science Laboratory, University College London, Holmbury St Mary, Dorking, Surrey RH5 6NT

² Department of Astronomy and Astrophysics, The Pennsylvania State University, 525 Davey Laboratory, University Park, PA 16802, USA

MNRAS in press.

Accepted 2012 March 29. Received 2012 March 9; in original form 2011 September 26

ABSTRACT

We study the star forming regions in the spiral galaxy NGC 4321 (M100). We take advantage of the spatial resolution (2.5 arcsec FWHM) of the *Swift*/UVOT camera and the availability of three UV passbands in the region $1600 < \lambda < 3000\text{\AA}$, in combination with optical and IR imaging from SDSS, KPNO/H α and *Spitzer*/IRAC, to obtain a catalogue of 787 star forming regions out to three disc scale lengths. We use a large volume of star formation histories, combined with stellar population synthesis, to determine the properties of the young stellar component and its relationship with the spiral arms. The H α luminosities of the sources have a strong decreasing radial trend, suggesting more massive star forming regions in the central part of the galaxy. When segregated with respect to NUV-optical colour, blue sources have a significant excess of flux in the IR at $8\mu\text{m}$, revealing the contribution from PAHs, although the overall reddening of these sources stays below $E(B-V)=0.2$ mag. The distribution of distances to the spiral arms is compared for subsamples selected according to H α luminosity, NUV-optical colour, or ages derived from a population synthesis model. An offset is expected between these subsamples as a function of radius if the pattern speed of the spiral arm were constant – as predicted by classic density wave theory. No significant offsets are found, favouring instead a mechanism where the pattern speed has a radial dependence.

Key words: galaxies: spiral – galaxies: star formation – galaxies: general – galaxies: individual (NGC 4321) –

1 INTRODUCTION

Ninety years after the Great Debate on the the nature of “spiral nebulae” (Shapley & Curtis 1921), our knowledge about disc galaxies has grown considerably. However, the processes responsible for their spiral appearance are still under scrutiny. Various mechanisms have been proposed, the widely accepted one being the triggering of a long-lived density wave that moves as a solid body, with constant pattern speed (Lin & Shu 1964). One can define the corotation radius as the point at which gas and stars move with the same speed as the spiral pattern. Since the rotation velocity of gas and stars is roughly independent of radius, the regions inside (outside) the corotation radius will move faster (slower) than the spiral arm pattern. The gas component piles up in the spiral arms, experiencing a shock that gives rise to star formation (Roberts 1969). One would expect in this scenario that the youngest stars born from the molecular clouds in the spiral arms would be found slightly ahead of the arm traced by the molecular gas, if located within the corotation radius, and behind the arm outside of corotation. Therefore, if we observe

the tracers of the different stages of star formation, such as HI, CO and H α , we expect to find an offset among them as a function of the radius. There are a number of observational efforts to detect such offset in the past (e.g. Vogel et al. 1988; García-Burillo et al. 1993; Rand 1995), and more recently (e.g. Tamburro et al. 2008; Egusa et al. 2009; Foyle et al. 2011). The majority of these studies measure the angular offsets between CO as a tracer of star forming molecular clouds and H α and/or $24\mu\text{m}$ as a tracer of young stars. A time difference around a few Myr is found (e.g. Egusa et al. 2009, and references therein) between CO and H α . We note that HI is not necessarily a direct tracer of molecular cloud formation, as it often results from molecular gas dissociation caused by star formation activity (Allen et al. 1986; Young & Scoville 1991). A stronger constraint can be imposed if we target instead tracers that cover a wider range of ages for the distribution of recently formed sources. The use of UV light opens up this possibility, since stellar populations can be tracked over the first few hundred Myr (Foyle et al. 2011).

An alternative mechanism for the triggering of spiral arms involves self-gravitational instabilities (Goldreich & Lynden-Bell 1965; Toomre 1981) whose spiral features have much shorter

* Email: ferreras@star.ucl.ac.uk

Table 1. Log of *Swift*/UVOT observations of NGC 4321 used in this paper.

ObsID	Date	Exposure Time (s)		
		UVW2 1928Å	UVM2 2246Å	UVW1 2600Å
00035227001	2005/11/06	532.0	0	80.6
00035227002	2005/11/08	386.6	290.1	192.7
00035227003	2005/11/13	6832.3	5107.6	3414.5
00030365002	2006/02/08	673.6	505.6	332.2
00030365005	2006/02/10	1023.6	0	343.1
00030365006	2006/02/12	1092.1	390.6	0
00030365007	2006/02/14	939.6	704.6	462.1
00030365008	2006/02/17	998.0	745.0	486.2
00030365009	2006/02/18	17.8	0	0
00030365011	2006/02/20	595.4	298.5	98.4
00030365012	2006/02/21	325.6	244.6	160.9
00030365013	2006/02/24	543.2	405.2	266.8
00030365014	2006/02/26	519.2	387.2	253.0
00030365015	2006/02/28	769.2	578.2	377.9
00030365016	2006/03/02	443.4	332.4	159.9
00030365017	2006/03/05	701.3	505.6	331.2
00030365018	2006/03/12	1032.4	773.4	508.2
00030365019	2006/03/18	1103.4	827.4	542.7
00030365021	2006/03/27	1045.7	0	468.1
00030365023	2006/03/29	1780.2	0	1368.0
TOTAL (ks)		21.35	12.10	9.85
Effective TOTAL (ks)		21.28	11.95	9.74

lifetimes. Numerical simulations have not been capable of explaining the onset of a stable density wave with constant pattern speed, whereas short-lived spiral arms appear naturally (see e.g. Sellwood 2011; Fujii et al. 2011; Quillen et al. 2011; Wada et al. 2011; Grand et al. 2012). Other processes, like tidal interactions or star-formation induced structures have been proposed as well, leaving a different imprint on the properties of the underlying stellar populations (Dobbs & Pringle 2010).

In this paper we make use of the Ultraviolet/Optical Telescope (UVOT, Roming et al. 2005) on board the *Swift* spacecraft (Gehrels et al. 2004), to study in detail the star forming regions of a nearby grand-design spiral. NGC 4321 (M100) is a face-on late-type spiral galaxy (SABbc) towards the Virgo cluster (de Vaucouleurs et al. 1991). Even though *Swift* is an observatory built for the study of transient phenomena, most notably Gamma Ray Bursts, the resolution of UVOT makes it an optimal instrument to study star formation in nearby galaxies. The presence of a recent supernova in NGC 4321 (SN2006X, Suzuki & Migliardi 2006) triggered a number of follow-up observations with *Swift*/UVOT, allowing us to put together one of the deepest UV images of a nearby galaxy at a spatial resolution of 2.5 arcsec (FWHM) over a ~ 100 arcmin² field of view. In this paper we adopt the distance from the Hubble Space Telescope Key Project to measure Hubble’s constant (Freedman et al. 2001), with a distance modulus $\mu = 30.91 \pm 0.07$ mag, implying a distance of 15.2 Mpc, and an angular scale of 73.7 pc/arcsec. The scale length of the disc of NGC 4321 is $h=1.39$ arcmin or 6.15 kpc measured in the V band (Kodaira et al. 1986). We use this value as a characteristic disc length throughout this paper. The radial positions of the sources are deprojected by using an inclination of 38° , with the receding side located at a position angle of 151° (Chemin et al. 2006).

2 THE UV IMAGES

We extracted the UV images of NGC 4321 from the archive of the *Swift*/UVOT mission¹ at HEASARC. The log of the observations can be found in Table 1. UVOT is one of the three instruments on board the *Swift* observatory. It couples a 30 cm Ritchey-Chrétien telescope to a photon-counting, microchannel-plate-intensified CCD camera. Details of the instrument can be found in Roming et al. (2005), whereas the calibration is described in Poole et al. (2008) and Breeveld et al. (2010, 2011). We use the three available UV filters: UVW2, UVM2 and UVW1, that span the wavelength range: 1600-3400Å. These three filters roughly map the spectral window of the *GALEX* NUV passband (Martin et al. 2005), with UVM2 centered at the position of the 2175Å UV-bump in the Milky Way extinction curve (Conroy et al. 2010). Fig. 10 in Poole et al. (2008) shows the in-orbit effective area of the UVOT filters. The spatial resolution of the instrument, along with a Point Spread Function of 2.4, 2.5 and 2.9 arcsec (FWHM) in UVW2, UVM2 and UVW1, respectively (Breeveld et al. 2010), makes UVOT images significantly better resolved than NUV images with *GALEX*, which has a FWHM of ~ 6 arcsec (Morrissey et al. 2005). We note that at the distance of M100, the UVOT resolution limit maps a physical distance around 200 pc, which is the maximum possible value to be able to neglect deblending issues in HII regions, given their characteristic sizes (Kennicutt et al. 1989).

We retrieved the science-grade exposures from the archive. Some of these images did not have an aspect correction. This failure is often caused by the lack of nearby stars in the USNO catalogue, that are used as reference in an automatic way to determine this correction. In order to have as many images as possible, we wrote our own software to aspect correct the images from a manual selection of foreground stars, and to combine all images with a flux-conserving drizzling algorithm at the same pixel size (i.e. 0.5 arcsec), based on the method of Fruchter & Hook (2002). Some of the images, with exposure times typically below 30 seconds, could not be used because they could not be properly registered. Hence, we define as effective integration times those from the final exposure map within the footprint of NGC 4321. The exposure map in this region is homogeneous. The total effective exposure times of the UV data are 21.28ks in UVW2, 11.95ks in UVM2 and 9.74ks in UVW1. The top panels of Fig. 1 shows greyscale images of the UVOT combined exposures. We illustrate in Fig. 2 the difference between our UVOT/UVW2 deep exposure and the available archival image from *GALEX*/NUV (exposure time 1183 s). Both frames show the central 8×8 kpc² region.

The source detection was performed with SExtractor (Bertin & Arnouts 1996) on the UVW2 image, which is the deepest one of the three, and corresponds to the shortest wavelength – optimally mapping ongoing star forming regions. The SExtractor code has been optimized for the detection of sources over a homogeneous background (e.g. galaxies in a survey or stars in a globular cluster). However, our case is slightly different, as the star forming sources are located on top of a diffuse background that has to be removed before detecting the sources. To contend with this, we define our own background on the original UVW2 image, following a procedure inspired by the methodology set out in Hoversten et al. (2011). A number of images are obtained by performing a circle median of the observed image over a range of radii. In order to determine the background, we need to subtract the information over smaller scales, ranging from individual HII

¹ <http://heasarc.nasa.gov/W3Browse/>

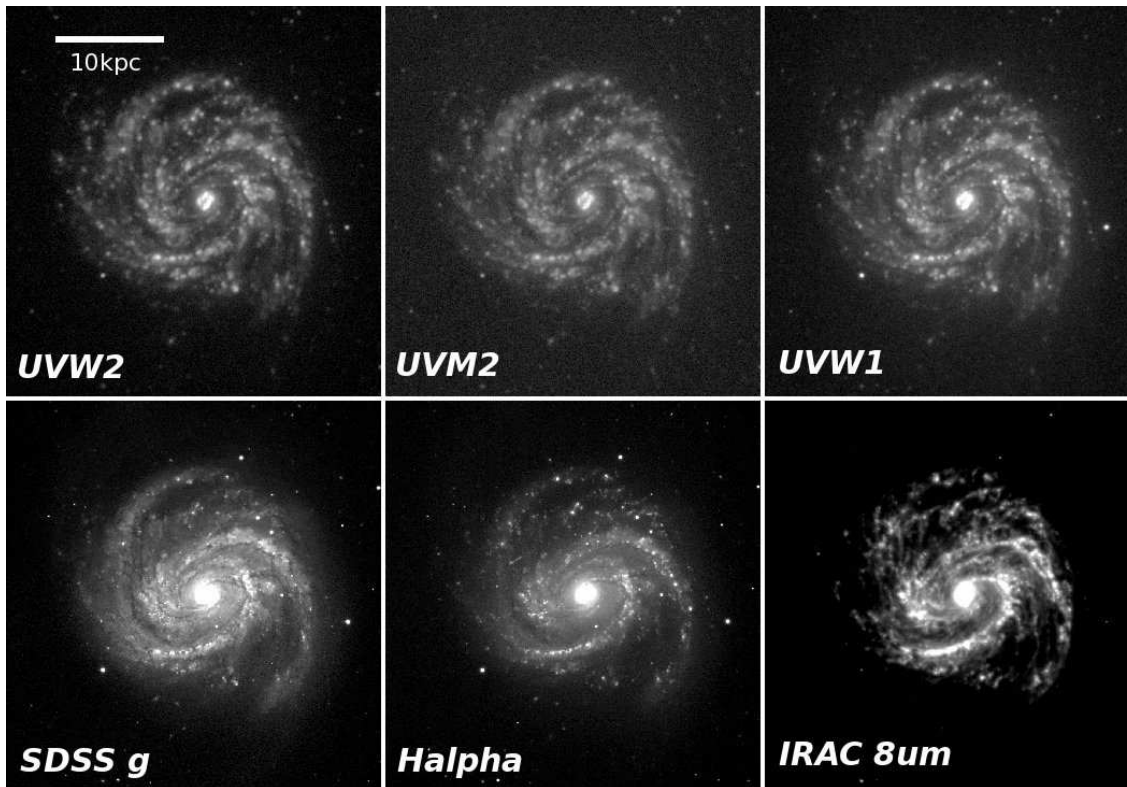


Figure 1. Views of NGC 4321 (M100) in different passbands over a 8×8 arcmin² field of view. North is up, East to the left. The top panels show deep NUV imaging with the *Swift*/UVOT instrument. The bottom panels show optical/IR images from archival data, as labelled.

regions to structures generated by the superposition of clustered, unresolved star forming sources (see Pleuss et al. 2000, for a detailed analysis of the effects of poorer spatial resolution). The spatial resolution (2.5 arcsec), pixel size (0.50 arcsec) and galaxy scale (74 pc/arcsec) of the images led us to choose the following radii for the median kernel: $R=\{5,10,15,20,25,30\}$ pixels, which map into a physical scale between 0.18 and 1.11 kpc. The smallest option maps scales over the largest sizes of HII regions (Scoville et al. 2001). We combine all those images along with the original one to determine, pixel by pixel, the background as the *minimum* pixel value among these images. Fig. 3 compares the UVW2 image with the background-subtracted one following this methodology. The selection criteria applied to SEXtractor, impose a detection threshold at a minimum of 9 connected pixels with a count rate 2σ above the background. The final catalogue comprises 787 sources out to $R=3h$. Fig. 4 shows the radial trend of the number density of NUV-detected sources, and those with available $H\alpha$ photometry – which amount to 68% of the total sample. Notice the level in the number counts around $R=2h$ (see also inset of Fig. 4), revealing a sharp truncation of the UV light tracing the youngest stellar populations in NGC 4321. The brightest $H\alpha$ sources, corresponding to stronger sites of star formation, are preferentially located in the central regions. We will discuss this issue in more detail in §4. The positions of the detected sources are used for the photometric analysis. Note the photometry is performed on the original image, not the background-subtracted one. Hence, the photometry can be described as a superposition of a young, star forming region, and an older component from the background populations.

Since UVOT is a photon counter, its photometric accuracy for brighter sources is limited by the sampling rate of the CCD, which

is 91 frames per second. Bright sources will experience a coincidence loss effect, whereby the true flux is underestimated as all photons hitting the detector in a single frame and within a small region, are counted as one. This effect has been properly characterized in Poole et al. (2008) and Breeveld et al. (2010), and is especially important with the optical passbands, where the photon count rate is much higher (as opposed to the UV, see Fig. 1 of Hoversten et al. 2011, to illustrate this point).

In our case, optical photometry is available from the Sloan Digital Sky Survey (see §3), so only the UV data from UVOT is used. For the UV images we apply the corrections defined in Poole et al. (2008). Our photometric measurements are performed within a $R=3$ arcsec aperture (see §3). For the integration times of the final images, the *Swift*/UVOT exposure time calculator² gives point-source detections at $S/N \sim 5$ of $UVW2=23.6$, $UVM2=22.80$ and $UVW1=22.7$ (AB), in good agreement with our photometric data: Using the detection of a 5σ fluctuation above the background within the extent of a PSF FWHM, we obtain limiting magnitudes in the final images of $UVW2=23.5$, $UVM2=23.2$, and $UVW1=22.9$ (AB). Fig. 5 translates the $UVW2=23.5$ limit into a stellar mass limit as a function of age – according to the simple stellar populations from the 2009 version of the Bruzual & Charlot (2003) models for a Chabrier (2003) Initial Mass Function. Both dustless and a dusty, $E(B-V)=0.2$ mag model are considered. The inset shows the distribution of UVW2 sources, with a vertical line marking the $S/N=5$ detection limit. A comparison of photometric measurements between *GALEX*/NUV (see Fig. 2) and UVOT/UVM2 – which is the filter that tracks best the throughput of the NUV pass-

² http://www.mssl.ucl.ac.uk/www_astro/uvot

Table 2. Photometry of UVW2 selected sources in NGC 4321¹: *Swift*/UVOT and SDSS (optical).Table 2. Photometry of UVW2 selected sources in NGC 4321¹: *Swift*/UVOT and SDSS (optical).

ID	$\Delta RA(^{\circ})$	$\Delta Dec(^{\circ})$	UVW2	UVM2	UVW1	SDSS u	SDSS g	SDSS r	SDSS i	SDSS z
001	-0.060	-0.052	16.39±0.08	16.06±0.10	16.08±0.09	15.67±0.06	15.02±0.09	14.64±0.09	14.54±0.12	14.38±0.15
002	+0.116	+0.015	17.28±0.10	16.94±0.11	16.81±0.14	16.18±0.07	15.30±0.08	14.83±0.08	14.61±0.13	14.39±0.10
003	-0.012	+0.137	16.63±0.07	16.33±0.09	16.34±0.08	15.88±0.07	15.08±0.06	14.62±0.10	14.42±0.10	14.22±0.14
004	-0.120	+0.098	16.86±0.09	16.46±0.10	16.40±0.08	15.79±0.08	14.86±0.07	14.41±0.06	14.16±0.06	13.92±0.06
005	-0.201	-0.118	19.79±0.14	19.56±0.12	19.35±0.13	18.84±0.10	17.53±0.09	16.88±0.09	16.58±0.10	16.42±0.11
006	+0.198	-0.291	21.13±0.13	20.80±0.12	20.73±0.06	20.09±0.08	18.84±0.08	18.20±0.09	17.91±0.11	17.77±0.10
007	-0.171	+0.344	20.15±0.06	19.75±0.06	19.62±0.08	19.37±0.10	18.54±0.09	17.79±0.08	17.45±0.07	17.14±0.08
008	+0.120	-0.406	22.03±0.13	21.84±0.19	21.53±0.19	20.95±0.20	19.68±0.16	18.88±0.13	18.46±0.09	18.17±0.09
009	-0.147	-0.339	20.40±0.07	20.10±0.07	19.98±0.07	19.43±0.06	18.52±0.06	17.94±0.05	17.68±0.06	17.47±0.07
010	+0.193	+0.313	20.52±0.13	20.20±0.12	20.02±0.14	19.45±0.10	18.39±0.11	17.87±0.09	17.61±0.13	17.48±0.12
011	-0.280	-0.227	19.93±0.09	19.64±0.08	19.55±0.09	19.22±0.08	18.64±0.07	18.06±0.08	17.86±0.10	17.70±0.10
012	+0.109	-0.436	21.76±0.08	21.56±0.12	21.26±0.13	20.40±0.10	19.38±0.12	18.75±0.11	18.49±0.11	18.23±0.13
013	-0.077	-0.405	20.44±0.12	20.15±0.14	19.98±0.12	19.71±0.09	18.74±0.09	18.17±0.10	17.94±0.09	17.79±0.07
014	-0.304	+0.372	21.90±0.13	21.31±0.09	21.00±0.10	20.91±0.18	20.43±0.32	19.33±0.12	18.98±0.09	18.67±0.07
015	+0.104	-0.466	21.92±0.09	21.94±0.19	21.50±0.14	20.87±0.12	19.81±0.12	19.06±0.13	18.85±0.15	18.66±0.15
016	+0.140	-0.470	22.10±0.09	22.23±0.15	21.77±0.19	21.04±0.09	20.20±0.16	19.46±0.15	19.10±0.11	18.89±0.12
017	-0.134	+0.475	21.27±0.10	20.97±0.06	20.71±0.07	19.96±0.07	18.85±0.06	18.43±0.06	18.26±0.07	18.14±0.08
018	+0.425	+0.001	22.39±0.13	21.68±0.18	21.75±0.13	20.58±0.12	19.66±0.18	19.02±0.12	18.75±0.14	17.74±0.08
019	+0.440	+0.024	22.73±0.30	21.88±0.63	22.10±0.55	20.93±0.15	20.00±0.25	19.32±0.18	19.03±0.19	17.87±0.10
020	+0.434	-0.259	21.72±0.07	21.43±0.17	21.25±0.12	20.60±0.17	20.42±0.20	19.95±0.26	19.68±0.20	19.86±0.25
021	-0.409	+0.362	22.01±0.18	21.77±0.16	21.31±0.10	20.47±0.09	20.49±0.16	19.63±0.09	19.60±0.10	19.49±0.08
022	+0.244	-0.523	22.30±0.09	22.01±0.12	21.92±0.09	21.32±0.09	20.59±0.15	20.53±0.12	20.74±0.20	—
023	+0.074	-0.553	21.62±0.10	21.30±0.12	21.15±0.10	20.91±0.11	19.80±0.11	19.54±0.09	19.39±0.14	19.21±0.14
024	+0.499	-0.170	20.82±0.08	20.43±0.12	20.38±0.18	19.70±0.14	19.11±0.08	18.94±0.07	18.85±0.06	18.96±0.06
025	-0.306	+0.552	23.36±0.20	22.93±0.22	22.94±0.33	21.47±0.09	20.63±0.14	21.07±0.53	21.43±0.63	—

¹ Photometry in the AB system, uncertainties quoted at the 1 σ level (random errors only). The co-ordinates are given as offsets, in arcminutes, with respect to the central position: RA=185.72833, Dec=+15.82194 (J2000.0). This is an excerpt of the full table that can be accessed in the electronic version of this paper.

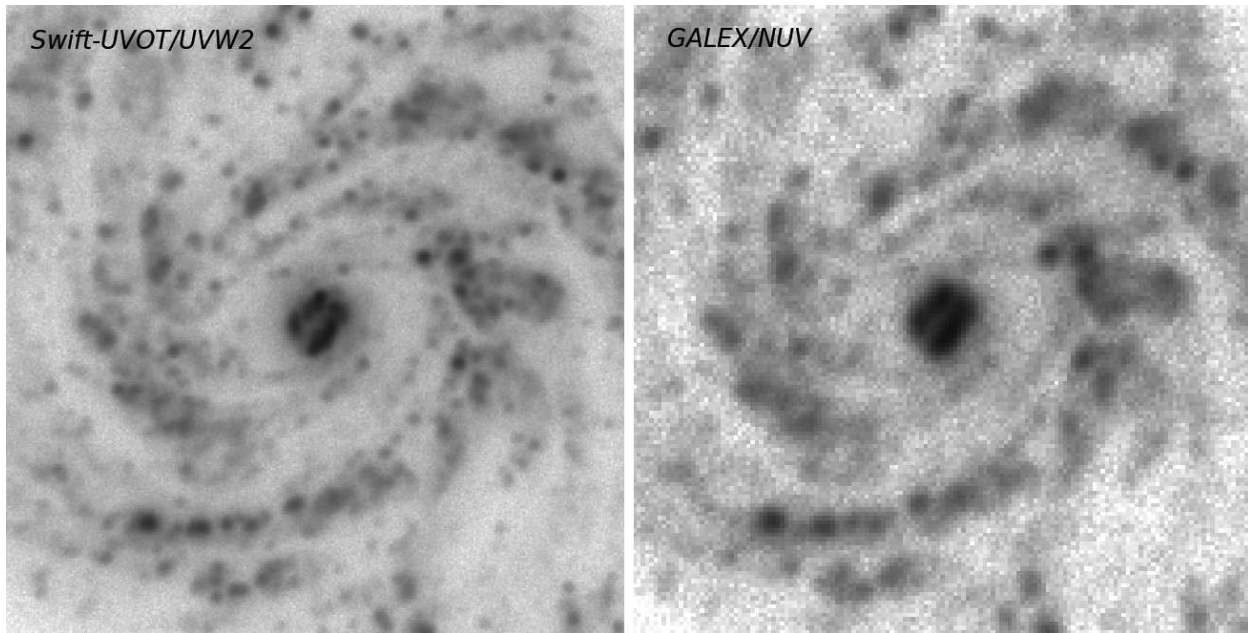


Figure 2. A comparison of the depth and resolution between our UV imaging (UVOT/UVW2, 21.3ks, left), and the available archival image from GALEX/NUV (1.1ks, right). Both frames show the central $8 \times 8 \text{ kpc}^2$ region.

band – gives good agreement, with an RMS scatter for the difference $\text{NUV} - \text{UVM2}$ around 0.18 mag (taking sources brighter than $\text{UVM2} = 22\text{AB}$). This scatter is mainly dominated by the fact that the measurements are taken over a crowded field.

3 A PANCHROMATIC VIEW OF NGC 4321

In addition to NUV data, we retrieved the optical images from the Sloan Digital Sky Survey/DR8 (Aihara et al. 2011). NGC 4321 falls at the intersection of four different SDSS fields (run=3631, field=456,457; and run=4381, field=99,100). We used the mosaic making facility from the SDSS-III Service Archive Server (<http://data.sdss3.org/mosaics>) to retrieve a properly calibrated image in all five bands (u, g, r, i, z) and registered the images. In addition, imaging is available from Spitzer/IRAC, and KPNO ($H\alpha$). The reduced, calibrated images are taken from the Fifth data delivery (April 2007) of the SINGS catalogue³ (Kennicutt et al. 2003). All the optical and IR images are re-sampled to a common size and pixel scale, given by the UVW2 frame, which is the image used for the selection of targets. We use the IRAF task *wregister* to ensure all bands are aligned properly and with the UVOT original pixel size (0.502 arcsec). We compared the photometric estimates before and after this transformation, to find no significant systematic change. Fig. 1 shows some of these frames, from the UV to the IR.

The photometry for all images (UV, optical and IR) is performed with our own code, described below, motivated by the need for a consistent background subtraction and error estimate. For each position, determined by the SExtractor run, we measure the flux within a $R=3$ arcsec aperture. At every pixel the background is estimated within a circular region with radius $R=20$ arcsec, where all pixels already allocated to a source by SExtractor (i.e. on the segmentation map) are removed. This distribution is then clipped at

the 3σ level and the median of the resulting set is taken as the background. The IRAC measurements include standard aperture corrections as prescribed in the instrument handbook⁴. We note that the standard calibration of the UVOT instrument is done on photometric measurements of point sources within a $R=5$ arcsec aperture (Poole et al. 2008; Breeveld et al. 2010). Given the spatial resolution of the camera, this choice of aperture is optimal for the photometry of Gamma Ray Bursts – the main target of UVOT science. However, it does not take advantage of the spatial resolution in this case. Hence, we chose a smaller radius for the measurements ($R=3$ arcsec), and applied an aperture correction to align with the standard calibration. This correction is obtained by performing aperture photometry on a number of isolated stars in the frame. We selected five bright unresolved targets, for which the photometry is compared between a $R=3$ arcsec and a $R=5$ arcsec aperture. This result is extended to the SDSS, and NOAO/ $H\alpha$ frames, to correct for the difference in PSF between the different images. For the Spitzer/IRAC photometry, we already make use of the published aperture corrections, as explained above. The corrections for the UVW2, UVM2, UVW1 filters are 0.150, 0.215, and 0.168 mag, respectively. In contrast, the aperture corrections for the SDSS images are 0.030, 0.045, 0.092, 0.073, and 0.052 mag, in the $u, g, r, i,$ and z bands, respectively. Finally, the NOAO $H\alpha$ image needs a correction between these apertures of $\Delta \log H\alpha = 0.126$ dex. Tables 2 and 3 show an excerpt of the aperture corrected photometry for the sources in all Swift/UVOT, SDSS, KPNO/ $H\alpha$ and Spitzer/IRAC bands, with the error bars quoted at the 1σ level. The photometry in the tables is corrected for (Milky Way) foreground extinction according to the reddening law of Fitzpatrick (1999) for $E(B-V)=0.026$ towards the direction of NGC 4321, taken from the maps of Schlegel et al. (1998).

³ <http://sings.stsci.edu>

⁴ <http://irsa.ipac.caltech.edu/data/SPITZER/docs/irac/iracinstrumenthandbook/>

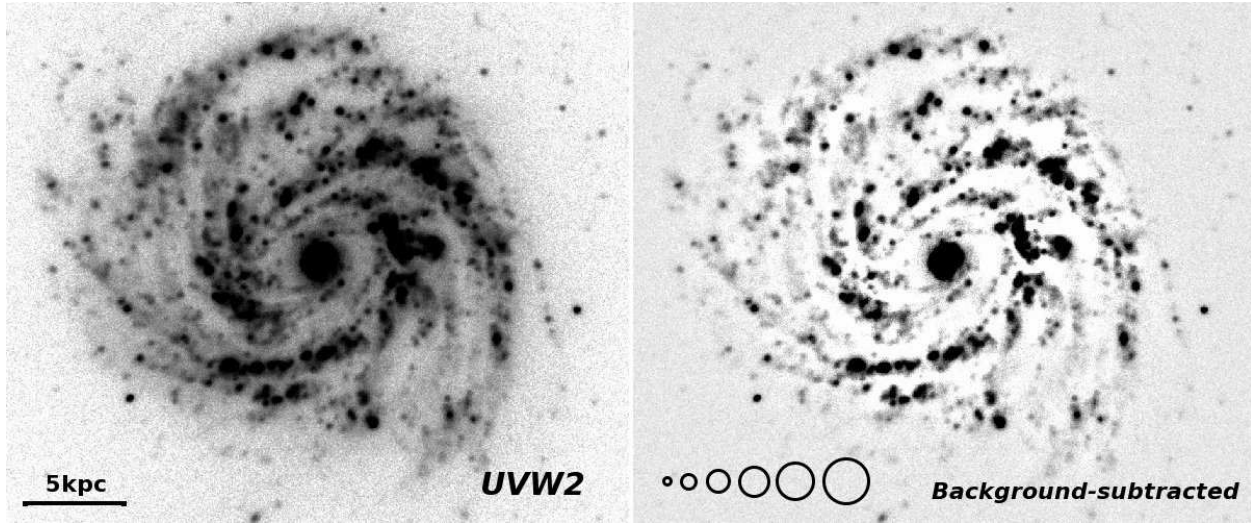


Figure 3. Illustration of our background subtraction method. The scale is the same for both images. The circles are the apertures used for the selection of the background at a given point (see text for details).

Table 3. Photometry of UVW2 selected sources in NGC 4321¹: Spitzer/IRAC and H α .

ID	R/h	[3.6 μ m]	[4.5 μ m]	[5.8 μ m]	[8 μ m]	log H α [†]
001	0.072	13.19±0.09	13.06±0.10	12.27±0.07	11.05±0.07	2.31±0.04
002	0.103	13.02±0.12	12.91±0.11	12.05±0.14	10.81±0.15	2.06±0.07
003	0.104	13.02±0.10	12.89±0.09	12.23±0.07	11.02±0.05	2.44±0.03
004	0.116	12.68±0.07	12.59±0.08	11.88±0.06	10.68±0.06	2.16±0.05
005	0.212	15.50±0.12	15.47±0.10	15.08±0.09	13.99±0.07	—
006	0.254	16.96±0.13	16.97±0.10	16.95±0.12	16.60±0.22	0.26±0.08
007	0.276	15.79±0.08	15.60±0.06	14.76±0.09	13.49±0.06	1.32±0.07
008	0.309	17.25±0.07	17.30±0.08	16.90±0.07	15.81±0.09	0.24±0.33
009	0.312	16.34±0.09	16.29±0.07	15.40±0.07	14.23±0.09	0.94±0.07
010	0.320	16.58±0.14	16.44±0.13	15.98±0.10	14.86±0.11	0.86±0.08
011	0.327	16.46±0.10	16.33±0.08	15.12±0.08	14.00±0.08	1.25±0.06
012	0.330	17.38±0.09	17.44±0.08	17.11±0.10	15.90±0.09	0.34±0.07
013	0.331	16.80±0.08	16.75±0.09	16.22±0.08	15.08±0.07	0.87±0.03
014	0.349	17.03±0.13	16.79±0.11	15.61±0.12	14.31±0.09	1.16±0.03
015	0.352	17.80±0.14	17.85±0.09	17.42±0.11	16.24±0.11	-0.04±0.28
016	0.358	17.82±0.13	17.80±0.14	17.19±0.15	15.76±0.17	-0.00±0.22
017	0.361	17.42±0.14	17.42±0.16	18.18±0.88	20.61±1.19	-0.96±0.08
018	0.370	17.97±0.11	17.93±0.15	18.67±0.62	—	0.70±0.06
019	0.387	18.35±0.23	18.40±0.17	19.34±0.68	—	0.74±0.04
020	0.391	17.81±0.15	17.46±0.16	16.77±0.16	15.77±0.59	0.85±0.17
021	0.406	17.33±0.10	17.03±0.06	15.40±0.09	14.10±0.08	1.25±0.08
022	0.415	—	—	18.78±0.43	16.55±0.45	—
023	0.417	18.56±0.22	18.81±0.28	—	—	—
024	0.428	17.75±0.12	17.56±0.12	16.45±0.14	15.22±0.17	0.82±0.06

¹Photometry for the IRAC bands in the AB system, uncertainties quoted at the 1 σ level (random errors

only). This is an excerpt of the full table that can be accessed in the electronic version of this paper.

[†] measured as $\log_{10}[L(H\alpha)/10^{37}\text{erg/s}]$.

4 MODELLING THE STELLAR POPULATIONS

Fig. 6 shows the NUV and optical colours of the UVW2-selected sources. A number of colour-colour diagrams are shown, involving UVOT and SDSS photometry. The observations (dots) match the predictions for a set of simple stellar populations (SSP). All models have solar metallicity. The thick solid orange lines correspond to dustless SSPs from the latest models of Bruzual & Charlot (2003), with a Chabrier (2003) initial mass function (IMF). To illustrate

the effect of using a different population synthesis model, or a different IMF, we also show in the figure the colour tracks from the Starburst99 dustless models (Leitherer et al. 2010) with a Salpeter (1955) IMF (blue dashed lines). For reference, crosses mark stellar ages of 1, 100, 500 and 900 Myr in the latter. We also include, as a thin solid red line, the effect of a E(B–V)=0.2 mag dust screen on the Bruzual & Charlot models, according to a Milky Way reddening law (Fitzpatrick 1999). The use of this reddening law is justified by the type of dust present in NGC 4321 (see e.g. Draine et al.

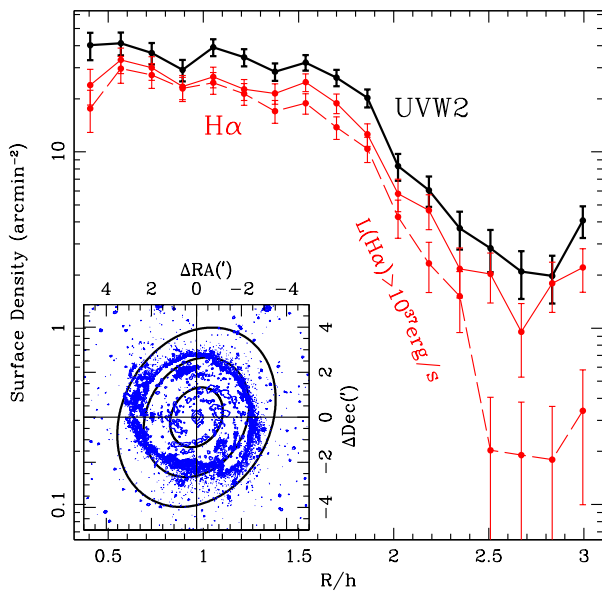


Figure 4. Radial profile of the surface density of UVW2 sources (thick black line), including the density of counterparts in the H α images (red). The surface density of bright H α sources ($L(\text{H}\alpha) > 10^{37} \text{erg/s}$) is shown as a dashed red line. The error bars give the Poisson fluctuations. The inset shows the extent of the UVW2 disc, with projected circles – according to the orientation of the disc – representing the $R=h$, $2h$, $3h$ radii, where h is the characteristic scale-length measured in the V-band (Kodaira et al. 1986)

2007). The model predictions clearly do not favour large amounts of dust, as expected from a UV-based source detection. Notice that on the colour-colour diagrams the dust content of the sources is found within a small range of $E(B-V) \lesssim 0.2 \text{ mag}$. We will quantify this statement in some detail below. Fig. 6 also reveals that the age of these sources is never older than about 1 Gyr, although we have to take care of the presence of background populations of older stars. Note the UV colours are in better agreement with the SSP models, whereas the optical colours are more dispersed. This is caused by the contribution at redder wavelengths from older populations within the apertures. We explore this issue in more detail in the next figure.

Fig. 7 shows the trend of the H α luminosities with respect to UVW2 magnitude, for those sources with a detection in the H α image (68% of the total sample). H α emission in star forming regions originates from gas excited by ionising photons from OB stars, i.e. more massive than $\sim 15M_{\odot}$. In contrast, NUV emission will also originate from the photospheres of lower mass stars, down to $\sim 3M_{\odot}$. Hence, the ratio between H α and NUV light works as a stellar clock over the first few million years of the nascent population (assuming a universal initial mass function, as expected for a bright galaxy, see Hoversten & Glazebrook 2008). The solid lines in the top panel of Fig. 7 correspond to the model predictions from Starburst99 for a simple stellar population at solar metallicity, with a Kroupa IMF (see Leitherer et al. 2010, and references therein). The Kroupa IMF is very similar to the Chabrier IMF used below for the analysis of the photometry: differences between them at the level of the data used are indistinguishable and do not affect our conclusions. The three solid lines represent three different stellar masses, from 10^3 to $10^5 M_{\odot}$. As age progresses, the H α flux decreases: the crosses, from top to bottom, mark the ages of 1, 5 and

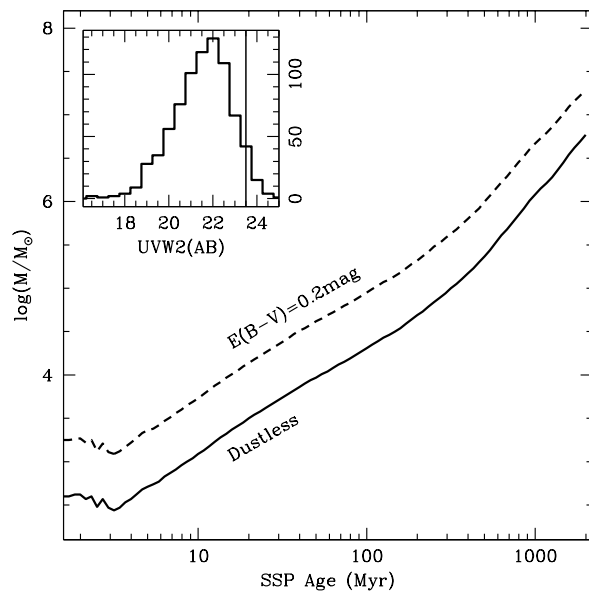


Figure 5. The stellar mass is shown with respect to the age of a simple stellar population for the limiting magnitude of UVW2=23.5 (at $S/N \sim 5$). Dustless (solid) and a dusty case (dashed) is considered, as labelled. The inset shows the histogram of UVW2 detections, with the vertical line locating the $S/N \sim 5$ case.

10 Myr. The star forming sources are coded according to radial position. To highlight the differences with respect to galactocentric distance, we show those sources with $R < h$ (solid red dots) or $R > 2h$ (open blue dots). The radial trend is evident, with the central sources being more massive, a result consistent with the findings of Goddard et al. (2011). Notice the orientation of the “dust vector” for $E(B-V)=0.2 \text{ mag}$. If dust were an important factor in the inner regions (i.e. the solid red dots), the segregation between central and outer sources in this graph would be more prominent, as a reddening correction would shift the points corresponding to the central regions towards the right of the figure, therefore increasing the separation between inner and outer sources. The ages of all sources are mostly younger than 10 Myr, as expected for an H α detection. The bottom panels show the optical colours, with the solid lines representing the Starburst99 predictions for the same models as in the top panels. Differences with respect to the radial distance are less evident, with a tail towards bluer colours in the outer sources. Those sources with colours redder than those from the simple stellar populations reflect the contribution from an underlying older component, which will dominate optical and NIR light. This figure illustrates the shortcomings of simple stellar populations in describing the photometric data.

The simplest model to overcome this problem involves a superposition of two SSPs. These models have been applied for the detection of residual star formation over the old populations found in early-type galaxies (see e.g. Ferreras & Silk 2000; Kaviraj et al. 2007). The models we use in this paper are described by five free parameters comprising the age of the old and young components (t_{O} and t_{Y} , respectively), the metallicity of both populations (assumed to be the same), the mass fraction in young stars (f_{Y}) and the dust reddening affecting the young component (E_{Y}), whereas the old component is considered to be dustless. In order to determine robust best fits, we opted for a full search of this five dimen-

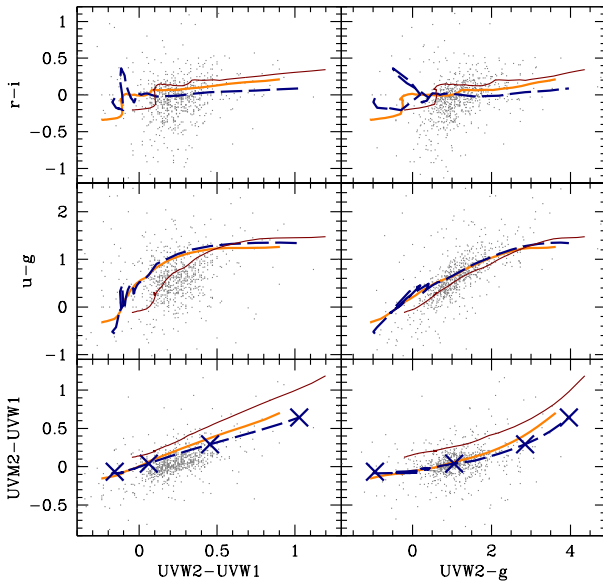


Figure 6. Colour-colour diagrams of the star forming regions in NGC 4321. The observed magnitudes have already been corrected for foreground extinction ($E(B-V)=0.026$). The models correspond to dustless CB09 (thick solid line, orange), SB99 (dashed line, blue) and CB09 with a $E(B-V)=0.2$ mag dust screen (thin solid, red). See text for details. The SB99 models in the bottom panels are marked by crosses for ages (from left to right) of 1, 100, 500 and 900 Myr.

sional parameter space. The grid of parameters is shown in Table 4, involving over 100 million models. We compute the flux from the SSPs, integrated over the filter response functions, and store them in a lookup table, to maximise the computing speed of the fitting algorithm, which is also parallelized to reduce wall-clock computing time. The effect of dust on the magnitudes is modelled by a fourth order polynomial in $E(B-V)$, where the coefficients are computed from a grid of 16,384 SSP models over a range of ages, metallicities and $E(B-V)$, using a Fitzpatrick (1999) reddening law. For each choice of parameters, the photometric data from the UVOT, SDSS and IRAC channels 1 (central wavelength $\lambda_c = 3.6\mu\text{m}$) and 2 ($\lambda_c = 4.5\mu\text{m}$) are used to define a likelihood. Following a Bayesian approach, we apply a Gaussian prior on the metallicity, with mean $\log Z/Z_\odot = -0.1$ and standard deviation 0.3 dex. The choice of mean is based on the observations of the gas-phase metallicity of M100 (Moustakas et al. 2010). However, we note that by removing the prior altogether, the age distribution of the old and young components is not affected within the scatter found among the sources.

Fig. 8 shows the distribution of the ages – total mass weighted average (*top*) or age of the youngest component (*bottom*) – and dust reddening for all sources with respect to UV-optical colour or UV flux. The big dots track the median of the distribution within bins keeping equal number of sources per bin, with the error bars representing the RMS scatter. Solid (open) dots correspond to sources at radial distance from the centre $R < h$ ($R > 2h$). As expected, UV-optical colour tracks the age of the young component and no significant trend is found with respect to the dust, obtaining a value for the reddening around $E(B-V) \lesssim 0.2$ mag. The distribution of metallicities has a mean of $\log Z/Z_\odot = -0.18$ – as expected, slightly lower than the measured gas-phase metallicity – and an

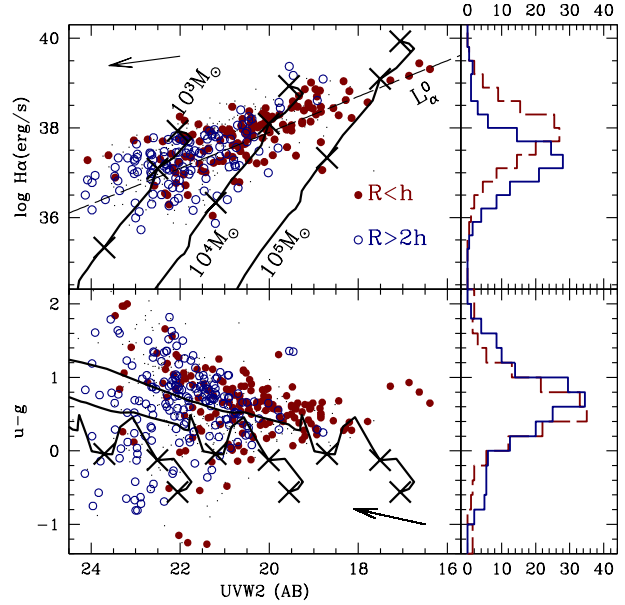


Figure 7. The $H\alpha$ line luminosities and optical colours of the star forming regions are shown with respect to UVW2 magnitudes. The star forming regions are split with respect to galactocentric distance, as labelled. The lines track the predictions from Starburst99 (Leitherer et al. 2010) of a simple stellar population with solar metallicity, and stellar masses between 10^3 and $10^5 M_\odot$. The crosses mark (from top to bottom) ages of 1, 5 and 10 Myr. The panels on the right show the distribution of inner (dashed) and outer (solid) star forming regions. The arrows in both panels correspond to a dust attenuation of $E(B-V)=0.2$ mag using a Milky Way reddening law. The dashed line in the top panel marks a limiting line luminosity $\log L_{H\alpha}^0(\text{erg/s}) \equiv 37.9 - 0.4(\text{UVW2}_{\text{AB}} - 20)$, used as a proxy to segregate $H\alpha$ detected sources with respect to age (see Fig. 11).

RMS scatter of 0.08 dex. There is no significant radial trend in metallicity, although the RMS scatter is higher at $R > 2h$ (0.12 dex). Note that the ages of the young component found here are significantly older than those estimated from the $H\alpha$ luminosities (Fig. 7), reflecting the complex mixture of populations within a resolution element (see e.g. Pleuss et al. 2000). Within a UVOT detection, we expect to have a wide range of stellar populations, including dust obscured regions, $H\alpha$ emitting sources, and more mature UV-bright areas. An analysis based on the broadband photometry will be inherently biased towards the last component. The presence of dust obscured regions can be illustrated by the stacking of sources into two representative UV-to-IR spectral energy distributions (SEDs). Fig. 9 shows the photometric SEDs of the youngest sources (using the UVW2-g colour as a proxy for age) have an IR excess in the IRAC bands, which reflects the contribution from dust-obscured regions that are possibly too faint in the UV-optical range to have an effect on the analysis of the UVOT/SDSS photometry. However, this figure gives further support to the use of UVW2-g as a proxy for the stellar ages of these sources. Notice in Fig. 8 the lack of any trend in the properties of the stellar populations with respect to radial distance, except for the fact that the outer sources are fainter in UV (see also Fig. 7), confirming that the radial change refers to the stellar mass content of the sources. The young component has a distribution of ages in the range 10–100 Myr. We will use this information in the next section to explore in detail the distribution of UV sources with respect to the spiral arms.

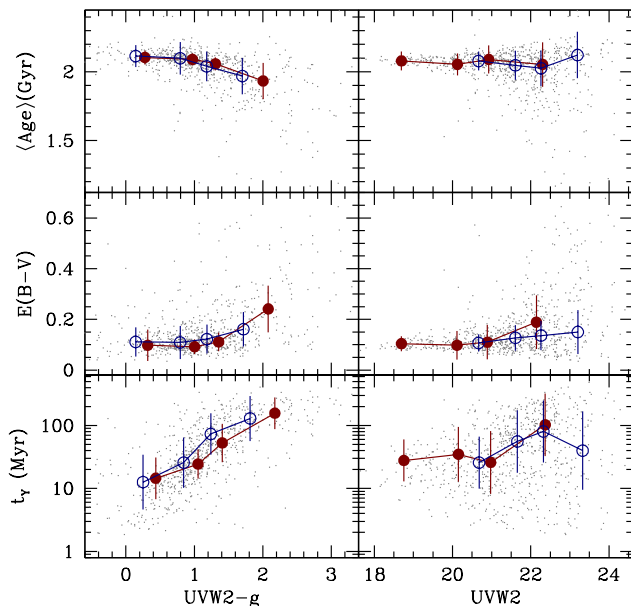


Figure 8. Distribution of ages and dust reddening of the UV sources according to the two-burst model (see text for details). The solid (open) dots show median values for subsamples at $R < h$ ($R > 2h$), with the binning chosen at equal number of sources per bin. The error bars correspond to the RMS scatter of individual sources within each bin. The top panels show the mass-weighted average age, whereas the bottom panels correspond to the age of the youngest component in the two-burst model adopted here (see text for details).

5 PUTTING DENSITY WAVE THEORY TO THE TEST

The properties of the underlying stellar populations of the star forming sources provide valuable constraints on the origin of spiral arms. In the previous section, we showed that our NUV-detected sources span a wide range of stellar ages (a few hundreds of Myr) and are distributed over a large range of galactocentric radii. Therefore, they represent an ideal tracer for the “offset method” (see e.g. Egusa et al. 2009), to look for variations in the distribution of different star formation tracers around the spiral arms. Standard density-wave theory predicts a systematic trend in the distribution of stellar ages inside and outside of the corotation radius. Foyle et al. (2011) used UV images from *GALEX* and IRAC/ $3.6\mu\text{m}$ emission to trace older populations. However, NGC 4321 is not in their sample and the spatial resolution of UVOT is superior to *GALEX*.

In order to analyse the properties of the star forming sources with respect to the spiral arms, we fit three portions of the spiral structure of NGC 4321 in regions where the arms can be traced. Fig. 10 shows the selection of the UV sources along the spiral arms. We use the UVW2 and the $H\alpha$ images to manually select a number of points along the spiral arms. The solid lines tracing the arms in Fig. 10 are obtained from a linear interpolation of these sources in polar coordinates. The crosses, triangles and circles locate the UVW2 sources that reside within ± 2 kpc of the spiral arms.

Fig. 11 (left) shows a sketch of the changes expected in the distribution of the spiral arm offsets of the star forming sources with respect to age and galactocentric distance. The solid blue and dashed red distributions illustrate the trend of the offsets between a very young component (e.g. an HII region) and an older one

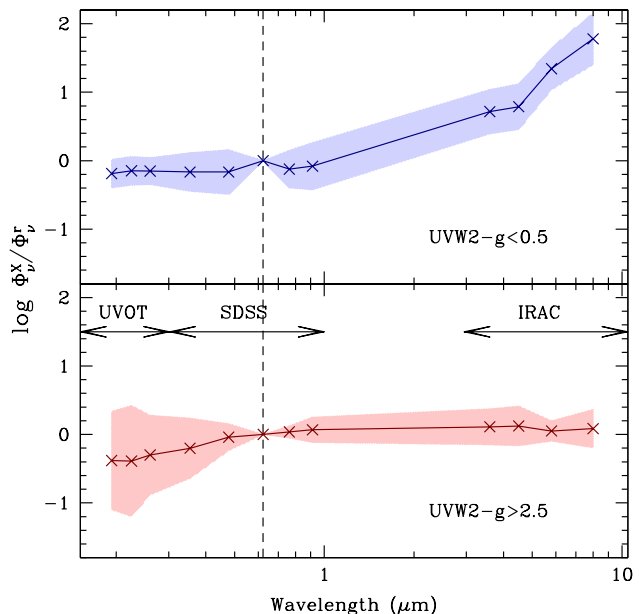


Figure 9. Spectral Energy Distribution of a subsample, selected according to UVW2-g colour as labelled. The lines and shaded areas map the average and standard deviation of all sources within the colour selection, shown as the flux through an “X” band representing the filters from UVOT to IRAC, as shown in the horizontal axis, measured as a ratio with respect to the SDSS r flux. The blue sources (top panel) have a clear excess towards longer wavelengths, possibly from PAH dust emission.

(e.g. an UV star forming source), respectively. The telltale sign of a density wave with constant pattern speed would be the shift of the older component with respect to the young one inside and outside corotation. We emphasize here that we only focus on *relative* offsets between these two components, noting that there would be an additional, smaller, offset between the HII regions and the molecular gas, as found in, e.g. Tamburro et al. (2008). The histograms on the right hand side of Fig. 11 show observed distributions of various properties of the sources with respect to the distance to the spiral arm for two choices of radial separation, at either side of the corotation radius suggested by Canzian & Allen (1997) (top panels: $R > 1.5h$; bottom panels: $R < h$). They compared the two dimensional observed velocity field with what the first-order linear spiral density wave theory predicts, and measured a corotation radius $R_{\text{cor}} = 98 \pm 10$ arcsec (shown for reference in Fig. 10). We note that this estimate, located around $R \sim 1.5h$ falls in the middle of our distribution of sources. We will adopt this value for reference in our analysis, although we note that other studies give higher results: Sempere et al. (1995) propose a corotation radius in the range 8–11 kpc, corresponding to 100–150 arcsec. The pattern speed measured by Rand & Wallin (2004), using the Tremaine-Weinberg method, implies a corotation radius of ~ 2 arcmin (Egusa et al. 2009), while Oey et al. (2003) suggest a corotation radius of 2.6 arcmin. However, these methods may not be applicable if the spiral arm pattern speed changes as a function of radius. For instance, Meidt et al. (2009) applied their developed version of the Tremaine-Weinberg method and demonstrated that some spiral galaxies show a radial variation of the spiral pattern speed. Unfortunately, NGC 4321 is not in their sample.

The left and central panels are model-independent compar-

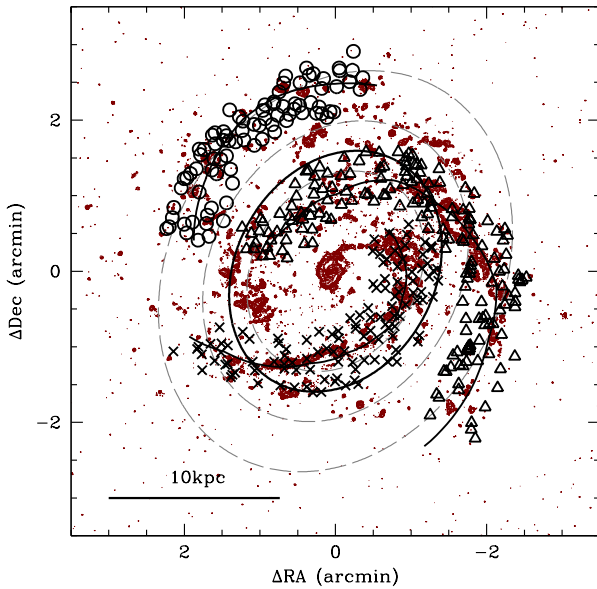


Figure 10. The $H\alpha$ sources are used to define three portions of the spiral arm structure where we can study the distribution of star forming sources. The contour map shows, as reference, the UVW2 image, which tracks a wider range of stellar ages. The dashed projected circles have radii h , $3h/2$, and $2h$, where h is the disc scale-length. The thick solid circle locates the corotation radius according to Canzian & Allen (1997). The crosses, triangles and circles are the UVW2 sources located within ± 2 kpc of the definition of the arms.

isons of NUV-detected sources with respect to their $H\alpha$ luminosity or UV–optical colour, respectively. The $H\alpha$ selection is split at a reference value for the luminosity of the line defined by $\log L_{\alpha}^0(\text{erg/s}) \equiv 37.9 - 0.4(\text{UVW2}_{\text{AB}} - 20)$, motivated by the location of the $H\alpha$ sources in the top panel of Fig. 7. Hence L_{α}^0 acts as a $H\alpha$ -based tracer of stellar age. The middle panel is motivated by the broadband photometric analysis (see Figs. 8 and 9) but does not rely on any modelling. Finally, the rightmost panels separate the sample according to the ages of the young components according to this analysis, and described in the previous section. No significant offsets are found in any of these cases.

The lack of an offset is clearly inconsistent with a solidly rotating spiral arm pattern as predicted by density wave theory. Dobbs & Pringle (2010) show a predicted distribution of young star clusters with different ages from their numerical simulations with a fixed spiral arm potential rotating solidly and mimicking a long-lived spiral arm. Their fig. 4 provides a quantitative plot of the sketches we outlined on the left of our Fig. 11 and they consider alternative mechanisms for the formation of spiral arms that would give rise to similar distributions as our observed histograms. Interestingly, Egusa et al. (2009) also found no offset between CO and $H\alpha$ spiral arms in NGC 4321, although we note that their analysis covered a narrower radial range ($R < 1.4'$, roughly one scale length). In combination with our analysis, we can therefore state that in NGC 4321 no offset is found out to 2 scale lengths over a wide range of ages, from molecular clouds to about 100 Myr young stars. This is a striking result and agrees with what is also found in Foyle et al. (2011) for other galaxies. Our result provides further evidence against classic spiral density wave theory.

The distributions found in Fig. 11 can be naturally explained

if the spiral arm is “corotating” with the stars and the gas, i.e. if the spiral pattern speed decreases with galactocentric radius. Recent numerical simulation studies (Wada et al. 2011; Grand et al. 2012) claim that such corotating spiral arms are more naturally developed in numerical simulations. Indeed, it is rather difficult to reproduce the spiral density wave theory in numerical simulations with self-gravity (Sellwood 2011). Such corotating spiral arms suffer from the winding problem, but are found to be disrupted within a time-scale of a few hundreds of Myr (see e.g. Fujii et al. 2011; Quillen et al. 2011; Sellwood 2011, and references therein) and a snapshot of the evolving galaxy at any time always shows some spiral arm structure. Wada et al. (2011) also demonstrate that in such corotating spiral arms gas falls into the spiral arms both from behind and the front of the spiral arm and collides, inducing star formation in the arm. This scenario is consistent with the observed distribution of star forming sources presented here.

6 CONCLUSIONS

The resolution of the *Swift*/UVOT camera makes it an optimal instrument to explore the young star forming sources in nearby late-type galaxies. In combination with optical photometry, it is possible to disentangle the contribution from the more diffuse, older component, giving an estimate of the age and dust content of the young stars responsible for the NUV emission. In this study, we combine deep UVOT imaging in the NUV with optical and IR archival imaging to study the properties of 787 star forming regions in the spiral structure of NGC 4321, out to $R \sim 3h$. We find a strong trend of brighter $H\alpha$ sources in the central regions (Fig. 7, see also Goddard et al. 2011), whereas the ages, or the dust content of the star forming regions do not present a measurable correlation with galactocentric distance (Fig. 8), suggesting that the strong trend in $H\alpha$ flux is caused by a larger number of massive star forming sources in the central regions (assuming a universal stellar initial mass function). The presence of dust is revealed when stacking up the photometric SEDs of the sources according to their NUV–optical colour, with significant excess at $8\mu\text{m}$ for the bluest (and youngest) ones (Fig. 9). However, a quantitative analysis of the dust reddening from the photometric data gives rather low “spatial resolution averaged” values of $E(B-V) \lesssim 0.2$ mag. The main outcome of the comparison with stellar populations is that one can use UVW2–g colours as a proxy of the age of the younger component, ranging from a few Myr to a few hundred Myr (see Fig. 8).

The properties of these sources enable us to study the effect of the spiral structure, a powerful test of pattern formation in disc galaxies. The standard scenario of density wave theory with a constant pattern speed results in an offset with respect to age for the distribution of distances to the spiral arms as one moves from the central regions – where the gas moves faster than the pattern – to the outer disc (see Fig. 11, left). The advantage of UV imaging over studies based on comparisons between the gas component and HII/24 μm regions is the wider time baseline spanned by UV light, roughly of order 100 Myr. No significant differences are found in the distribution of these sources, giving further negative evidence for density wave spirals. Our findings reject the possibility that the results from Egusa et al. (2009) – giving no offsets between CO and $H\alpha$ over a narrower range ($R < 1.4'$) – can be explained by a radial coincidence with corotation. Instead, a scenario with short-lived corotating spiral arms is compatible with the data. Such structures have been found in numerical simulations of spiral galaxies

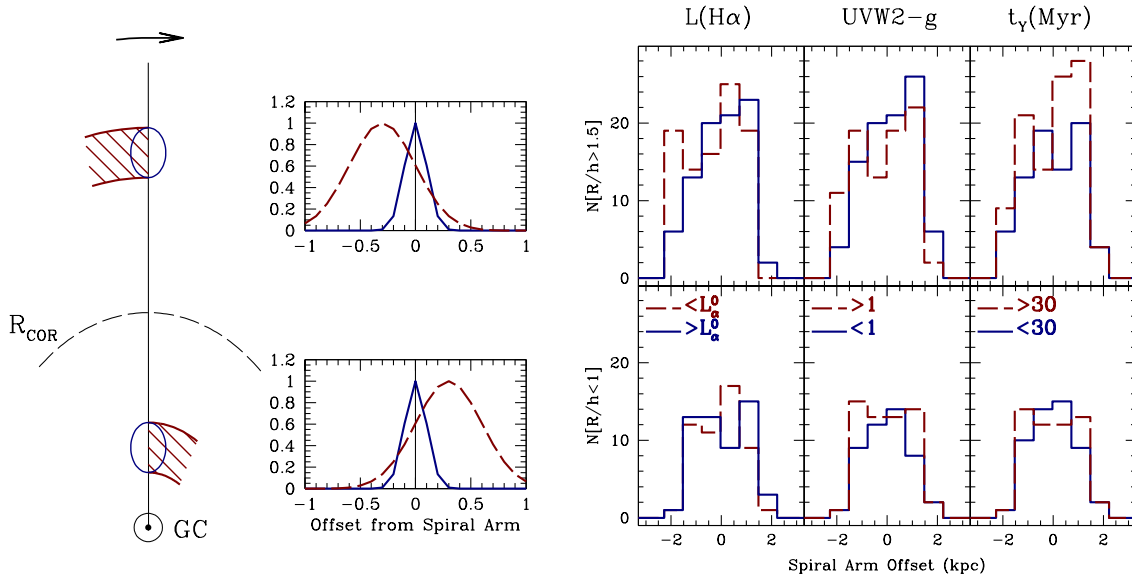


Figure 11. *Left:* Sketch of the expected shifts in the distribution of stellar populations according to density wave theory. A spiral pattern with constant angular speed – represented by the vertical line – interacts in different ways with the rotating gas depending on whether the gas is located inside or outside the corotation radius R_{COR} . On the left panels, a comparison of very recent star formation – as tracked by $H\alpha$ (solid blue curves) – with older stars – from UV light (dashed red curves) betrays the presence of a pattern in solid body rotation. *Right:* Comparison between the distribution of UVW2-selected sources split according to $H\alpha$ line luminosity ($L(H\alpha)$, leftmost panels), UV-optical colour (UVW2–g, middle panels) or the age of the young component (t_Y , rightmost panels), estimated from the modelling of the NUV/Optical/IR photometry. The threshold in $H\alpha$ luminosity, L_{α}^0 , is defined with respect to the UVW2 flux in Fig. 7. Only sources within ± 2 kpc from the three spiral arms defined in figure 10 are included in the histograms, split according to radial distance to the centre, measured in disc scale lengths.

Table 4. Grid of 2-population models used in the analysis

Parameter	Young SSP	Old SSP	Models
Age (Gyr)	$-3 < \log t_Y < 0$	$0 < \log t_O < +1.12$	64×64
Metallicity (Z_{\odot})	$-2 < \log Z < +0.3$		24
Dust Reddening	$0 < E_{B-V} < 1$	dustless	32
Mass fraction	$0 < f_Y < 0.8$	$1 - f_Y$	32
TOTAL			1.007×10^8

(see e.g. Grand et al. 2012), implying a fundamental change of our views from the traditional concept of long-lived spiral arms.

ACKNOWLEDGMENTS

We would like to thank the MSSSL *Swift*/UVOT team for useful help on the data reduction of the UV datasets. The constructive criticism of the anonymous referee has greatly helped in improving this paper.

Funding for SDSS-III has been provided by the Alfred P. Sloan Foundation, the Participating Institutions, the National Science Foundation, and the U.S. Department of Energy Office of Science. The SDSS-III web site is <http://www.sdss3.org/>. SDSS-III is managed by the Astrophysical Research Consortium for the Participating Institutions of the SDSS-III Collaboration including the University of Arizona, the Brazilian Participation Group, Brookhaven National Laboratory, University of Cambridge, University of Florida, the French Participation Group, the German Participation Group, the Instituto de Astrofísica de Canarias, the Michigan State/Notre Dame/JINA Participation Group, Johns Hop-

kins University, Lawrence Berkeley National Laboratory, Max Planck Institute for Astrophysics, New Mexico State University, New York University, Ohio State University, Pennsylvania State University, University of Portsmouth, Princeton University, the Spanish Participation Group, University of Tokyo, University of Utah, Vanderbilt University, University of Virginia, University of Washington, and Yale University.

REFERENCES

- Aihara, H., et al. 2011, *ApJS*, 193, 29
 Allen, R. J., Atherton, P. D., Tilanus, R. P. J., 1986, *Nature*, 319, 296
 Bertin, E. & Arnouts, S., 1996, *A&AS*, 117, 393
 Breeveld, A. A., et al. 2010, *MNRAS*, 406, 1687
 Breeveld A. A., Landsman W., Holland S. T., Roming P., Kuin N. P. M., Page M. J., 2011, *AIPC*, 1358, 373
 Bruzual, G., Charlot, S., 2003, *MNRAS*, 344, 1000
 Canzian, B., Allen, R., 1997, *ApJ*, 479, 723
 Chabrier, G., 2003, *PASP*, 115, 763

- Chemin, L., et al. 2006, MNRAS, 366, 812
- Conroy, C., Schiminovich, D., Blanton, M. R., ApJ, 718, 184
- de Vaucouleurs, G., de Vaucouleurs, A., Corwin, H. G., Bata, R. J., Paturel, G., Fouqué, P., 1991, *The Third Reference Catalogue of Bright Galaxies*, Springer, New York
- Dobbs, C. L., Pringle, J. E., 2010, MNRAS, 409, 396
- Draine, B. T., et al., 2007, ApJ, 663, 866
- Egusa, F., Kohno, K., Sofue, Y., Nakanishi, H., Komugi, S., 2009, ApJ, 697, 1870
- Ferreras, I., Silk, J., 2000, ApJ, 541, L37
- Fitzpatrick, E. L., 1999, PASP, 111, 63
- Foyle, K., Rix, H.-W., Dobbs, C. L., Leroy, A. K., Walter, F., 2011, ApJ, 735, 101
- Freedman, W. et al. 2001, ApJ, 553, 47
- Fruchter, A. S., Hook R. N., 2002 PASP, 114, 144
- Fujii, M. S., Baba, J., Saitoh, T. R., Makino, J., Kokubo, E., Wada, K., 2011, ApJ, 730, 109
- García-Burillo, S., Guelin, M., Cernicharo, J., 1993, A & A, 274, 123
- Gehrels, N., et al. 2004, ApJ, 611, 1005
- Goldreich, P., Lynden-Bell, D., 1965, MNRAS, 130, 125
- Goddard, Q. E., Kennicutt, R. C., Ryan-Weber, E. V., 2011, MNRAS, 412, 1246
- Grand, R. J. J., Kawata, D., Cropper, M., 2012, MNRAS, 421, 1529
- Hoversten, E. A., Glazebrook, K., 2008, ApJ, 675, 163
- Hoversten, E. A., et al., 2011, AJ, 141, 205
- Kaviraj, S., et al. 2007, ApJS, 173, 619
- Kennicutt, R. C., Edgar, B. K., Hodge, P. W., 1989, ApJ, 337, 761
- Kennicutt, R. C., et al., 2003, PASP, 15, 928
- Kodaira, K., Watanabe, M., Okamura, S., 1986 ApJS, 62, 703
- Leitherer, C., Ortiz-Otálvaro, P. A., Bresolin, F., Kudritzki, R.-P., Lo Faro, B., Pauldrach, A. W. A., Pettini, M., Rix, S. A., 2010, ApJS, 189, 309
- Lin, C. C., Shu, F. H., 1964, ApJ, 140, 646
- Martin, D. C., et al. 2005, ApJ, 619, L1
- Meidt, S. E., Rand, R. J., Merrifield, M. R., 2009, ApJ, 702, 277
- Morrissey, P., et al., 2005, ApJ, 619, L7
- Moustakas, J., Kennicutt, R. C., Tremonti, C. A., Dale, D. A., Smith, J-D T., Calzetti, D., 2010, ApJS, 190, 233
- Oey, M. S., Parker, J. S., Mikles, V. J., Zhang, X., 2003, ApJ, 126, 2317
- Poole, T. S., et al., 2008, MNRAS, 383, 627
- Pleuss, P. O., Heller, C. H., Fricke, K. J., 2000, A& A, 361, 913
- Quillen, A. C., Dougherty, J., Bagley, M. B., Minchev, I., Comarretta, J., 2011, MNRAS, 417, 762
- Rand, R. J., 1995, AJ, 109, 2444
- Rand, R. J., Wallin, J. F., 2004, ApJ, 614, 142
- Roberts, W. W., 1969, ApJ, 158, 123
- Roming, P. W. A., et al., 2005, Space Sci. Rev., 120, 95
- Salpeter, E. E. 1955, ApJ, 121, 161
- Schlegel, D. J., Finkbeiner, D. P., Davis, M., 1998, ApJ, 500, 525
- Scoville N. Z., et al. 2001, AJ, 122, 3017
- Sellwood, J. A., 2011, MNRAS, 410, 1637
- Sempere, M. J., García-Burillo, S., Combes, F., Knapen, J. H., 1995, A& A, 296, 45
- Shapley, H., Curtis, H. D., 1921, Bull. of the NRC, 2, 171
- Suzuki, S., Migliardi, M. 2006, IAU Circ., 8667
- Tamburro, D., Rix, H.-W., Walter, F., Brinks, E., de Blok, W. J. G., Kennicutt, R. C., Mac Low, M.-M., 2008, AJ, 136, 2872
- Toomre, A., 1981, in Fall S. M., Lynden-Bell D., eds, *The Structure and Evolution of Normal Galaxies*. Cambridge Univ. Press, Cambridge, p. 111
- Tremaine, S., Weinberg, M. D., 1984, ApJ, 282, L5
- Vogel, S. N., Kulkarni, S. R., Scoville, N. Z., 1988, Nature, 334, 402
- Young, J. S., Scoville, N. Z. 1991, ARA& A, 29, 581
- Wada, K., Baba, J., Saitoh, T. R., 2011, ApJ, 735, 1